ACS NANO
Cite This: ACS Nano 2018, 12, 12512−12522
www.acsnano.org

ARTICLE

Anisotropic Electron−Phonon Interactions in Angle-Resolved Raman Study of Strained Black Phosphorus

Weinan Zhu,[†,⊥] Liangbo Liang,[‡,⊥] Richard H. Roberts,[§] Jung-Fu Lin,[§,∥] and Deji Akinwande*[,†,§]

[†]Microelectronics Research Center, Department of Electrical and Computer Engineering, The University of Texas, Austin, Texas 78758, United States

[‡]Center for Nanophase Materials Sciences, Oak Ridge National Laboratory, Oak Ridge, Tennessee 37831, United States

[§]Department of Materials Science and Engineering, Texas Materials Institute, The University of Texas, Austin, Texas 78712-1591, United States

[∥]Department of Geological Sciences, Jackson School of Geosciences, The University of Texas, 2305 Speedway Stop C1160, Austin, Texas 78712-1692, United States

Supporting Information

ABSTRACT: **Few-layer black phosphorus (BP) with an in-plane puckered crystalline structure has attracted intense interest for strain engineering due to both its significant anisotropy in mechanical and electrical properties and its high intrinsic strain limit. Here, we investigated the phonon response of few layer BP under uniaxial tensile strain (∼7%) with *in situ* polarized Raman spectroscopy. Together with the first-principles density functional theory (DFT) analysis, the anisotropic Poisson's ratio in few-layer BP was verified as one of the primary factors that caused the large discrepancy in the trend of reported Raman frequency shift for strained BP, armchair (AC) direction in particular. By carefully including and excluding the anisotropic Poisson's ratio in the DFT emulations, we rebuilt both trends reported for Raman mode shifts. Furthermore, the angle-resolved Raman spectroscopy was conducted *in situ* under tensile strain for systematic investigation of the in-plane anisotropy of BP phonon response. The experimentally observed thickness and crystallographic orientation dependence is elaborated using DFT theory as having a strong correlation between the strain-perturbated electronic-band structure and the phonon vibration modes. This study provides insight, both experimentally and theoretically, for the complex electron−phonon interaction behavior in strained BP, which enables diverse possibilities for the strain engineering of electrical and optical properties in BP and similar two-dimensional nanomaterials.**

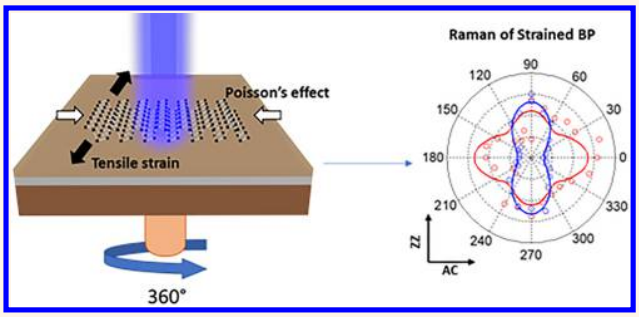

KEYWORDS: *black phosphorus, strain engineering, angle-resolved Raman spectroscopy, anisotropic Poisson's ratio, electron−phonon interactions*

Orthorhombic black phosphorus (BP) was rediscovered as a promising two-dimensional (2D) semiconductor for its tunable bandgap, fast carrier transport, and its buckled in-plane crystal structure that induces anisotropy in its electrical transport, optical emission, thermoelectric performance, and mechanical flexibility.[1−6] With effective dielectric encapsulation to enhance its ambient stability,[7,8] BP thin films have been actively employed in applications such as high speed and power-efficient flexible nano electronics,[1,5,9−12] quantum dot and memory devices,[13,14] and ultrafast photonics.[15,16] BP is particularly interesting for strain engineering owing to its in-plane anisotropy and its capability of sustaining high strain loading, with intensive theoretical studies having been done on tuning its mechanical, electronic, and optical properties.[17−22] The phonon vibration modes detected in Raman spectroscopy, which have been used for determining the crystallographic orientation of BP, are strongly correlated with the electronic band structure of BP and, thus, are theoretically projected to be highly sensitive under strain engineering.[23] A large discrepancy, however, remains in previously reported works for the trend of Raman

Received: September 11, 2018
Accepted: December 3, 2018
Published: December 3, 2018

DOI: 10.1021/acsnano.8b06940
ACS Nano 2018, 12, 12512−12522

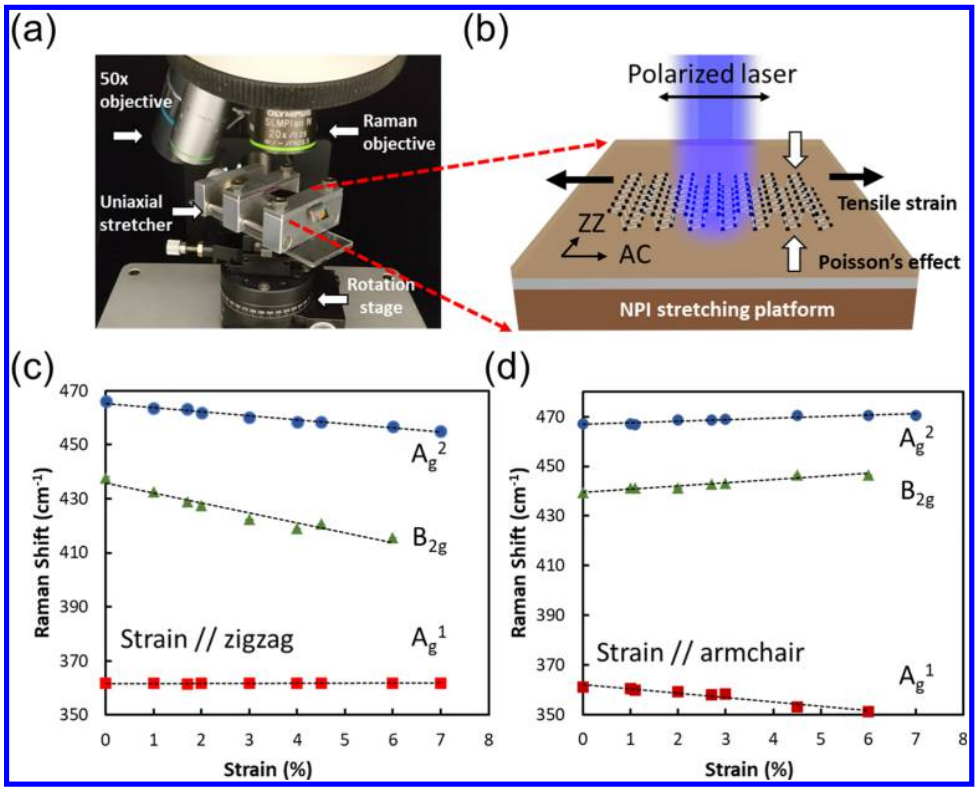

Figure 1. (a) Experimental setup for angle-resolved Raman characterization of few layer BP under uniaxial tensile strain. Uniaxial stretching fixture was mounted onto an automated rotation stage. Detailed setup information is elaborated in the Methods section. (b) Illustration of BP on polymeric substrate under tensile strain loading along AC direction. Poisson effect is illustrated as compressive strain perpendicular to the tensile strain loading. The Poisson's ratio for bilayer BP along the AC and ZZ directions were calculated from DFT simulations. (c) Statistics of Raman peak shifts of few-layer BP under tensile strain along ZZ direction. Red shifts of A_g^2 and B_{2g} modes were observed with average slope of ~−1.93 and −4.65 cm^{-1}/% strains, respectively. The A_g^1 mode exhibited negligible peak shift. (d) Statistics of Raman peak shifts of few-layer BP under tensile strain along the AC direction. The blue shift of A_g^2 and B_{2g} modes were observed with average slope ~1.61 and 2.39 cm^{-1}/% strains, respectively. A_g^1 mode exhibited a red shift with an average slope of ~−2.05 cm^{-1}/% strain.

frequency shift of BP under strain. Here in this work, we systematically studied the phonon response in BP thin films under uniaxial tensile strain loading up to 7% with *in situ* angle-resolved Raman spectroscopy for both thickness and crystallographic orientation dependence. First-principle density functional theory (DFT) simulation of the electronic band structure and phonon response in the strained BP validated that anisotropic Poisson's ratio along zigzag (ZZ) and armchair (AC) directions is one of the primary factors for the pre-reported discrepancy in strained BP Raman response. This systematic study of anisotropic Raman response of strained BP provided insight for the complex electron−phonon interactions and therefore enables diverse applications for strain engineering in the selective tuning of the electrical, optical, and thermal properties of BP and similar two-dimensional (2D) semiconductors.

RESULTS AND DISCUSSION

Theoretical studies of few-layer BP indicate a high strain limit of 27% (30%) of uniaxial tensile strain along the zigzag (armchair) directions.[24] The capability of sustaining such high intrinsic strain allows for a wide range of tunability in the electrical and mechanical properties. Significant phonon mode shifting and a semiconducting−metallic phase transition were theoretically predicted in BP thin films under sufficient strain loading.[24−27] Despite the promising predictions of strain tunability by theoretical studies, the realization of strain loading onto 2D crystals so far remains challenging. For highly stretchable substrate materials, such as PDMS, a large Young's modulus mismatch between the soft substrate and the stiff 2D semiconductors results in inefficient strain transfer.[28] Meanwhile, for flexible devices probing the electrical transport performance of BP thin films, the overall strain loading is strictly limited by the high-k dielectric materials with low critical strain limit (~2%), such as HfO_2 and Al_2O_3.[29,30] In this work, polymeric low-k dielectric was developed as a stretching substrate (Figure S1) that can achieve tensile strain reaching >7%.[31] With the help of PMMA encapsulation layer, NPI substrate with a Young's modulus of ~2.5 GPa can provide 100% efficiency in transferring tensile strain to the fully confined few-layer BP flakes and islands.[28,32] Using this polymeric substrate, the strain tunability of anisotropic electron−phonon and electron-photon interactions in BP thin films were systematically studied *in situ* with angle-resolved Raman spectroscopy. The experimental set up for *in situ* Raman characterization was shown in Figure 1a, with the stretching fixture mounted on an automated rotating stage. More detailed information on the experimental setup is provided in the Methods section.

Considering the anisotropic mechanical and electrical properties induced by the puckered honeycomb crystal structure, tensile strain was applied along the zigzag (ZZ) and armchair (AC) directions of BP, respectively. A linearly

DOI: 10.1021/acsnano.8b06940
ACS Nano 2018, 12, 12512−12522

Table 1. Raman Frequency Change Rate $\frac{\partial\omega}{\partial\varepsilon}$ (cm^{-1}/% Strain) of BP under Tensile Strain along the ZZ and AC Directions[a]

	ε // zigzag			ε // armchair			
$\partial\omega\partial\varepsilon$ (cm^{-1}/%)	A_g^1	B_{2g}	A_g^2	A_g^1	B_{2g}	A_g^2	ε_{max} (%)
experimental	0	−4.65 ± 1.66	−1.93 ± 0.88	−2.05 ± 0.60	2.39 ± 0.78	1.61 ± 0.32	7
DFT ($\nu \neq 0$)[b]	1.83	−8.17	−4.41	−2.69	0.79	0.78	
DFT ($\nu = 0$)	−0.61	−8.68	−3.92	−2.78	−0.85	−0.10	
experimental[33c]	~0	−2.3	−1.1	−1.3	0	0	2.8
experimental[34]	0.31	−3.0	−1.21	−1.37	0.28	0.50	1.77
experimental[35]	−0.52 ± 0.06	−10.92 ± 0.22	−4.32 ± 0.11	−3.81 ± 0.15	−1.85 ± 0.05	−0.03 ± 0.05	0.85
experimental[36]	−0.56	−5.46	−2.73	−1.37	−1.07	~0	0.17

[a]Experimental data and DFT calculated results (with and without Poisson's ratio ν) are listed. Experimental data from the literature are also included. [b]BP has anisotropic Poisson's ratio: $\nu = 0.85$ for ε // zigzag, while $\nu = 0.19$ for ε // armchair. [c]Note that the uniaxial strain in this work deviates from the zigzag or armchair direction by about 10−15°.

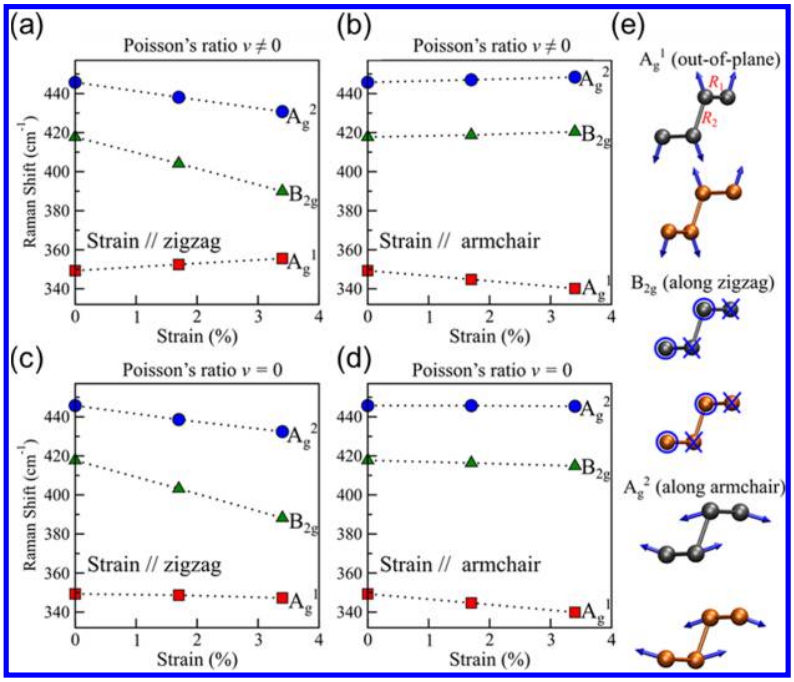

Figure 2. DFT calculated frequencies of A_g^1, B_{2g}, and A_g^2 modes as a function of the applied tensile strain along (a, c) ZZ and (b, d) AC directions of bilayer BP. When tensile strain is applied along one direction, compressive strain is usually induced along the perpendicular direction, which is described by the Poisson's ratio. In panels a and b, such an effect is considered with $\nu \neq 0$, while it is not considered in panels c and d with $\nu = 0$. (e) Blue arrows show vibrations of A_g^1 (primarily along the out-of-plane direction) and A_g^2 (primarily along the armchair direction), while blue circles and crosses indicate vibrations of B_{2g} coming out of and going into the page (*i.e.*, along the zigzag direction). R_1 and R_2 are the horizontal and vertical P−P bond lengths within a layer, respectively.

polarized 473 nm wavelength laser excitation was applied in the experiment with polarization aligned parallel to the strain loading direction. For the polarized Raman measurements, the analyzer is set parallel to the incident polarization direction. The representative Raman spectra of BP thin films under tensile strain are shown in Figure S2.

The Raman spectra of few-layer BP exhibit anisotropic responses in terms of both the Raman peak shifts and the polarization profiles when uniaxial tensile strain was applied along the ZZ and AC directions. The Raman peak shifts under strain originate from the alteration of the crystal lattice by tensile strain. Intuitively, tensile strain will result in the stretching of the bonds and, therefore, a softening of the phonon modes, which reflects in the Raman spectra as a red shift of the peak positions (*i.e.*, negative $\frac{\partial\omega}{\partial\varepsilon}$; for example, in the strained MoS_2).[28,37] As for BP with its anisotropic puckered structure, the effect of tensile strain on Raman peak shifts can be quite complex.[26,27,34−36] Here, we systematically investigate BP samples at different thicknesses with uniaxial tensile strain loading up to 7%, which is significantly higher than the strain applied in previous reports.[33−36] As shown in Figure 1c, a red shift was observed in the two in-plane modes, B_{2g} and A_g^2, when stretched along the ZZ direction, which indicates an effective P−P bond extension induced by the ZZ direction tensile strain. The slope of peak shift ($\frac{\partial\omega}{\partial\varepsilon}$) was estimated to be −4.65 ± 1.66 cm^{-1}/% strain for B_{2g} mode and −1.93 ± 0.87 cm^{-1}/% strain for the A_g^2 mode, respectively. The out-of-plane A_g^1 mode was negligibly affected by this in-plane tensile strain, as shown in Figure 1c. The case of uniaxial strain loading along the AC direction, shown in Figure 1d, is more complex; significant red shifting was observed in the out-of-plane A_g^1 mode ($\frac{\partial\omega}{\partial\varepsilon}$ = −2.05 ± 0.60 cm^{-1}/% strain), whereas a blue shift

DOI: 10.1021/acsnano.8b06940
ACS Nano 2018, 12, 12512−12522

was observed in both in-plane modes ($\frac{\partial\omega}{\partial\varepsilon}$ = 2.39 ± 0.78 cm^{-1}/% strain for B_{2g} mode and 1.61 ± 0.30 cm^{-1}/% strain for A_g^2 mode). In short, Figure 1c,d show that Raman shifts of B_{2g} and A_g^2 modes have the opposite response to the tensile strain along ZZ and AC directions (also see Table 1) and that the A_g^1 mode is much more sensitive to tensile strain along the AC direction. Furthermore, these trends do not change given the sample thickness varies from 3 to 30 nm. Thus, the strain can be also a reliable approach for identification of crystalline orientation of BP.[34]

Our results demonstrate that $\frac{\partial\omega}{\partial\varepsilon}$ can be either negative or positive depending on the Raman modes and the corresponding strain loading direction, consistent with prior works by Wang et al.[33] and Zhang et al.[34] (Table 1). In contrast, Li et al.[35] and Du et al.[36] reported negative $\frac{\partial\omega}{\partial\varepsilon}$values for all three modes under both the ZZ and AC directional tensile strains (Table 1). To understand why different strain behaviors were observed, first-principles density functional theory (DFT) calculations were carried out, demonstrating that the Poisson's ratio in BP thin films is the primary factor causing the discrepancy.[35,36] When tensile strain ε_1 is applied along one direction, the BP thin films tend to contract in the perpendicular direction (*i.e.*, compressive strain ε_2), and then the Poisson's ratio is defined as $\nu = -\frac{\varepsilon_2}{\varepsilon_1}$. Due to the in-plane anisotropy of BP, the Poisson's ratio changes with the direction of the uniaxial tensile strain: ν = 0.85 for ε // zigzag and ν = 0.19 for ε // armchair for 2L BP according to our calculations. If we ignore the lattice contraction perpendicular to the applied tensile strain direction, ν is fixed as 0. In the phonon calculations, the Poisson's ratio can be included ($\nu \neq 0$) and excluded ($\nu = 0$) to reveal its effect on $\frac{\partial\omega}{\partial\varepsilon}$. For 2L BP in Figure 2a,b, by considering the Poisson's ratio ($\nu \neq 0$), DFT calculations demonstrate the opposite response of A_g^1, B_{2g}, and A_g^2 modes to the tensile strain along ZZ and AC directions, in agreement with our experimental trends shown in Figure 1, the previous work by Zhang et al. (Table 1),[34] and a prior theoretical work with the effect of the Poisson's ratio included.[27] However, by excluding the Poisson's ratio (ν = 0) in Figure 2c,d, both the ZZ and AC directional tensile strains lead to softening of all three Raman modes, consistent with prior experimental works by Li et al.[35] and Du et al.[36] (Table 1) and the theoretical results without considering the Poisson's ratio by Zhang et al.[34] Note that the calculated numerical values of $\frac{\partial\omega}{\partial\varepsilon}$ are not in quantitative and perfect agreement with our experimental values, probably due to certain approximations adopted in the DFT methodology. In addition, DFT cannot model the exact experimental conditions. Nevertheless, it provides correct physical trends. Our calculations suggest that the Poisson's ratio is an important contributing factor for the differing experimental results reported in the literature because different strain engineering techniques can introduce different Poisson's ratios in the sample. In the prior experimental work by Li et al.,[35] the authors discussed that the strain induced to their BP samples through the experimental setup probably did not cause an effective in-plane contraction transverse to the applied strain direction (*i.e.*, the Poisson's ratio close to 0). In the work by Du et al.,[36] the maximum applied strain is only about 0.17%, which might not cause notable lattice contraction transverse to the applied strain direction, rendering the effective Poisson's ratio zero. In this work (with the strain up to 7%), the effect of the Poisson's ratio is validated by comparing experimental and theoretical data, and indeed, we observed the buckle delaminations due to contraction perpendicular to the tensile strain direction in the BP samples (Figure S3). The Poisson's ratio can also contribute to different theoretical results reported in literature. Note that similar calculations were carried out for monolayer and bulk BP (Figures S4 and S5) with similar results found, confirming that the strain dependence of the Raman mode frequencies is insensitive to the sample thickness, which also agrees with our experimental data. To summarize, by comparing our experimental and theoretical data with different results reported in literature (Table 1), we expect that the Poisson's ratio play an important role in explaining the discrepancy in reported experimental and theoretical works. However, we note that the applied uniaxial strain could deviate from the sample's armchair or zigzag direction by a certain degree and thus complicate the trends and values of $\frac{\partial\omega}{\partial\varepsilon}$for Raman modes in BP. This could also play a role in different results reported in literature. Furthermore, as shown in Table 1, the maximum applied strain (7%) in our work is notably larger than most prior works, which may enhance the effect of the Poisson's ratio in our samples. In other words, the large difference in the strain loadings in different experiments could also contribute to the discrepancy in the literature.

To gain further insight into the origin of these strain behaviors, we examined the phonon vibrations and BP's atomic structure under tensile strain. The top panel in Figure 2e shows two crucial structural parameters for BP: R_1 and R_2 are the respective horizontal and vertical P−P bond lengths within a layer. Table 2 summarizes their calculated change rates (Å/% strain) under the ZZ and AC directional tensile strains for 2L BP, with the cases of $\nu \neq 0$ and ν = 0. Starting from the scenario of ν = 0 because the lattice constant is increased in the tensile strain direction while the lattice constant in the perpendicular direction is fixed to the unstrained value, the bonds are generally stretched, as reflected by the positive change rates in Table 2 (except a very small negative value of R_2 under strain in the ZZ direction, but the increase of R_1 is much larger). Subsequently, the restoring forces are overall reduced, which can probably explain why $\frac{\partial\omega}{\partial\varepsilon}$are negative for all three modes under strain in both directions in Figures 1c and 2d as well as in previous works.[35,36] Once the effect of the Poisson's ratio is included ($\nu \neq 0$), the lattice contracts perpendicular to the tensile strain direction, thus, the changes of bond lengths become more complicated. As shown in Table 2 for $\nu \neq 0$, when tensile strain is applied along the ZZ direction, R_1 is noticeably increased but R_2 is decreased, which is similar to the case of ν = 0. However, the decrease rate of R_2

Table 2. Calculated Change Rates (Å/% Strain) of R_1 and R_2 for 2L BP under Tensile Strain along the Zigzag and Armchair Directions, With and Without Consideration of the Poisson's Ratio ν

	$\nu \neq 0$		$\nu = 0$	
strain direction	R_1 (Å/%)	R_2 (Å/%)	R_1 (Å/%)	R_2 (Å/%)
zigzag	0.0093	−0.0025	0.0101	−0.0013
armchair	−0.0010	0.0017	0.0009	0.0015

DOI: 10.1021/acsnano.8b06940
ACS Nano 2018, 12, 12512−12522

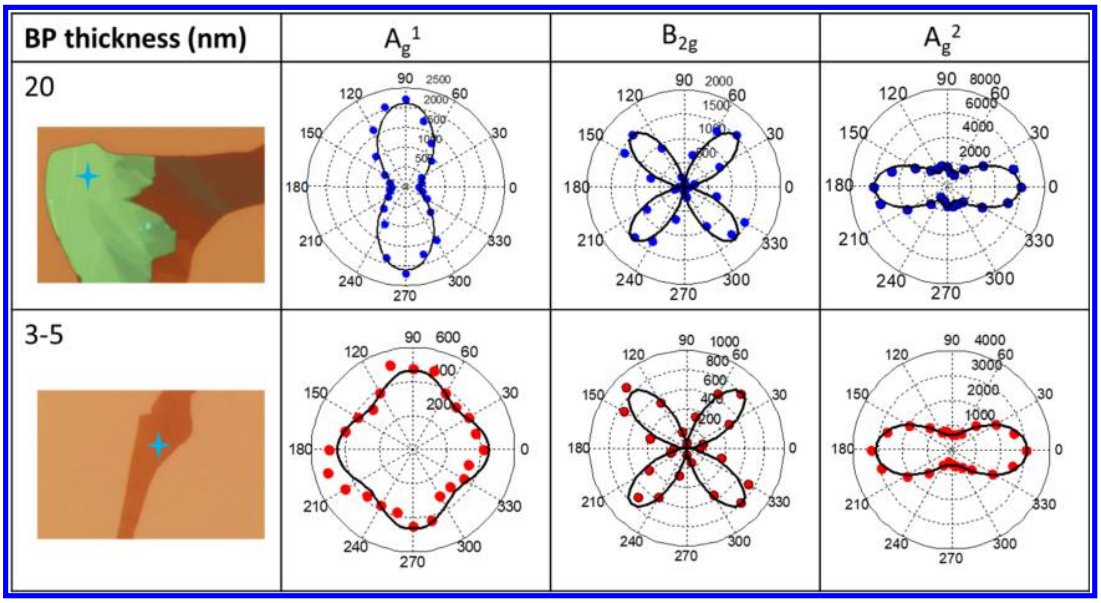

Figure 3. Typical categories of the BP flakes with distinct thickness showing anisotropic angle-resolved Raman characteristics. Incident laser wavelength is 473 nm under parallel configuration. Dots are experimental data, and black lines are the model fitting. 0° in the polar plot is defined along the AC direction.

nearly doubled the case of $\nu = 0$. The A_g^1 mode corresponds to a mainly out-of-plane vibration; hence, its frequency is mostly determined by R_2 with slight contribution from R_1 (Figure 2e). The doubled decrease rate of R_2 in the scenario of $\nu \neq 0$ enhances the overall restoring force, leading to a blue shift of the A_g^1 mode under the ZZ directional strain shown in Figure 2a. Moving to the B_{2g} and A_g^2 modes, which have atomic vibrations primarily along the in-plane zigzag and armchair direction (Figure 2e), respectively, their frequencies are influenced by both parameters R_1 and R_2. Because the number of horizontal P−P bonds is twice of the number of vertical P−P bonds in a layer, the change of R_1 should make a larger contribution to their frequency changes. As R_1 shows a much higher rate of increase than the decrease rate of R_2 (by a factor of 3.72; see Table 2), the overall restoring force is notably reduced for the B_{2g} and A_g^2 modes, resulting in their dramatic red shifts under the ZZ directional strain in Figure 2a. Due to the lower decrease rate of R_2, the blue shift of the A_g^1 mode is less dramatic in Figure 2a. However, when under tensile strain in the AC direction in the case of $\nu \neq 0$, R_1 is reduced, while R_2 is increased at a similar rate (Table 2). As discussed above, the A_g^1 frequency is dominated by R_2, while the B_{2g} and A_g^2 frequencies are more related to R_1. Therefore, the increase of R_2 leads to a red shift of the A_g^1 mode, but the decrease of R_1 leads to blue shifts of the B_{2g} and A_g^2 modes under the AC directional strain shown in Figure 2b. Our analysis here provides an atomic picture regarding the observed experimental trends in Figure 1 and the prior work by Zhang et al.[34]

Angle-resolved Raman was adopted for studying the in-plane anisotropy of strained few-layer black phosphorus.[38−40] As a reference, angle-resolved Raman were first collected on relaxed BP thin films with different thickness ranging from 3 to 20 nm while the Raman laser wavelength was fixed at 473 nm. All Raman spectra were collected under parallel configuration. The detailed experimental set up for the Raman system as well as the rotation stage is explained in the Methods section. The intensity profiles of the three characteristic Raman modes, A_g^1, B_{2g}, A_g^2 are shown in Figure 3. Under the laser line of 473 nm, B_{2g} and A_g^2 modes demonstrate little change in anisotropy for thin films with various thicknesses, in contrast with A_g^1 mode, in which salient differences including the reduction in the polarization dependence was observed when the thickness of BP films decreased from 20 to 3 nm. Here, 0 degree in all polar plots is set along the AC direction. The B_{2g} mode in all three samples shows consistent periodicity of 90° with the peak intensity occurring near 45°. Similarly, the A_g^2 mode, a mainly in-plane vibration along the armchair direction,[41] exhibits a dumbbell shape for all thicknesses examined with periodicity of 180°, and a maximum intensity occurred at 0°. The A_g^1 mode, which corresponds to primarily out-of-plane atomic oscillation,[41] exhibits strong thickness dependence. The clearly demonstrated dumbbell shape with periodicity of 180° was only observed in the thicker samples. In the sample with thickness below 5 nm, the polarization profile of the angle-resolved Raman intensity loses its dumbbell shape and becomes more isotropic with a much-reduced average intensity.

To better understand the thickness dependence in Raman intensity profiles and the anisotropic Raman scattering, Raman tensors of BP were derived here based on the complex dielectric tensors and phonon vibrations.[23,42] The complex Raman tensors of Raman active modes are given as:

$$R(A_g) = \begin{pmatrix} |a|e^{i\varnothing_a} & 0 & 0 \\ 0 & |b|e^{i\varnothing_b} & 0 \\ 0 & 0 & |c|e^{i\varnothing_c} \end{pmatrix}$$

$$R(B_{2g}) = \begin{pmatrix} 0 & 0 & |e|e^{i\varnothing_e} \\ 0 & 0 & 0 \\ |e|e^{i\varnothing_e} & 0 & 0 \end{pmatrix} \quad (1)$$

The corresponding Raman intensity under the parallel polarization configuration in the experimental backscattering geometry is therefore derived as:

DOI: 10.1021/acsnano.8b06940
ACS Nano 2018, 12, 12512−12522

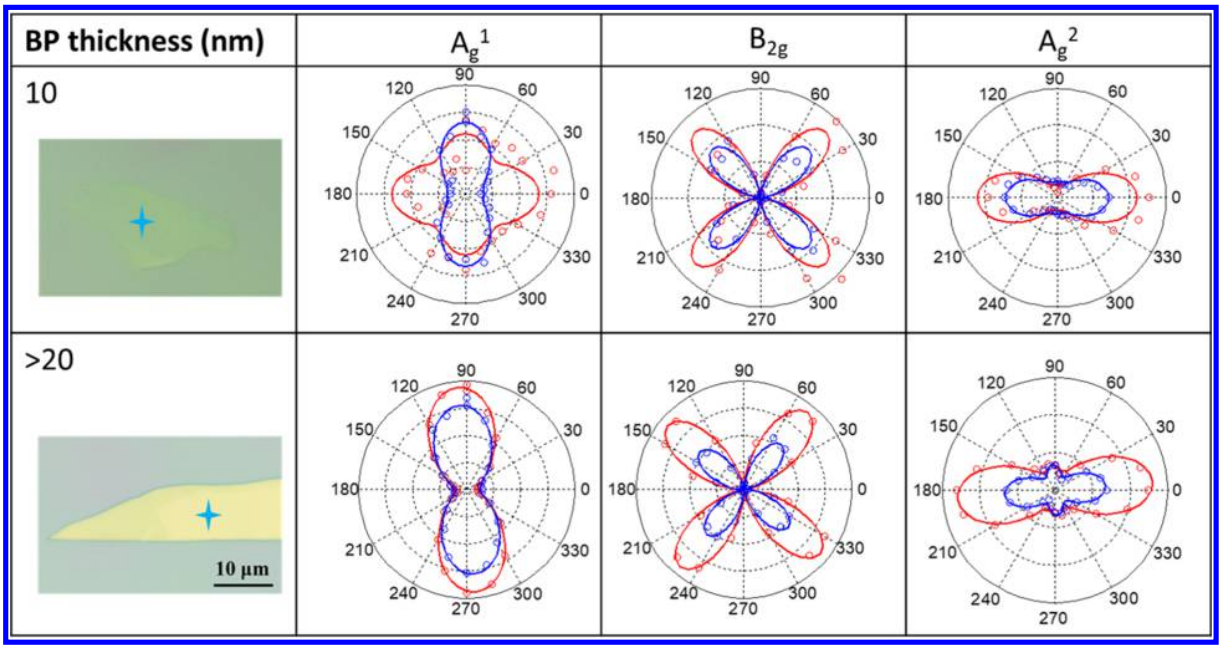

Figure 4. Under tensile strain along the ZZ direction, distinct angle-resolved Raman intensity evolution was observed in BP samples with different thickness. A dumbbell-shaped polarization profile for A_g^1 mode was reconstructed under tensile strain for BP sample with a thickness of ~10 nm. The red line and dots are the data collected for a relaxed sample under no stain. The blue line and dots are the data collected for sample under tensile strain. The strain loading for the two samples are 1.7% (10 nm) and 2% (>20 nm). Dots are experimental data, and lines are model-fitting results. 0° is defined along the AC direction in the polar plot.

$$I_{A_g}^{\parallel} = |(\sin\theta, 0, \cos\theta)\tilde{R}(\sin\theta, 0, \cos\theta)^T|^2$$
$$= \left|a|^2\left[\left(\sin^2\theta + \left|\frac{c}{a}\right|\cos\Phi_{ca}\cos^2\theta\right)^2 + \left|\frac{c}{a}\right|^2 \sin^2\Phi_{ca}\cos^4\theta\right]\right. \quad (2)$$

and

$$I_{B_{2g}}^{\parallel} = 4|e|^2\cos^2\theta\sin^2\theta \quad (3)$$

where θ is the angle of the laser polarization with respect to zigzag direction, and Φ_{ca} is the phase difference between the two Raman tensor element c and a.[42] Note that here we defined the X axis as the AC direction, Y axis as the out-of-plane direction, and the Z axis as the ZZ direction.[23,42] Thus, the Raman tensor element a (c) corresponds to the AC (ZZ) direction. The in-plane anisotropy of BP electron−phonon interactions is reflected in the Raman intensity polarization profiles of the A_g modes, which are directly determined by the absolute amplitude ratio $|c/a|$ and phase difference Φ_{ca}. The phase difference Φ_{ca} determines if there is a secondary maximum on the Raman polarization profiles. The value of $|c/a|$ determines whether the main axis in the polarization profiles is along the AC ($|c/a|<1$) or ZZ ($|c/a|>1$) direction. In addition, the more the $|c/a|$ value approaches 1, the less polarized the profile (*i.e.*, circular profile) observed. Extracted $|c/a|$ value for BP samples in Figure 3 were included in the Supporting Information. Comparison between A_g^1 and A_g^2 modes validated that the $|c/a|$ value determines the main axis of the polarization profiles. Under the experimental set up in this work, the main axis of in-plane A_g^2 mode tends to be along the AC direction (*i.e.*, $|c/a| < 1$) for all sample thicknesses studied. Because the A_g^2 mode primarily involves vibrations along the AC direction, the AC-direction component of the dielectric tensor generally has larger change by the A_g^2 vibrations than the ZZ-direction component, giving rise to the larger Raman tensor element in the AC direction (a) than in the ZZ direction (c).[6,23] However, the A_g^1 mode is mainly associated with out-of-plane atomic vibrations, and it does not show notable preference to the in-plane Raman tensor elements a and c. Therefore, its ratio of $|c/a|$ can be <1 or >1, depending on the thickness, consistent with the observed polarization profiles. The $|c/a|$ value of A_g^1 mode was approaching 1 while reducing the BP sample thickness. For the sample with a thickness of 3 nm, the value is 1.10 compared to 2.38 for the sample with a 20 nm thickness. Here in this work, the choice of 25 nm Al_2O_3/Si substrate did not impact on the anisotropic Raman response of BP samples with thickness much less than 25 nm, as the interference ratio from such substrate configurations is showing less than 3% of variance from the 300 nm SiO_2/Si substrate. The choice of laser energy and BP sample thickness are more critical factors in tuning the anisotropy in the angle-resolved Raman response of few-layer BP thin films. The interference ratio calculated for both type of substrates is included in Figure S8.

Employing the angle-resolved Raman spectroscopy under *in situ* tensile strain loading, we present the observations of the strong anisotropic and thickness-dependent Raman polarization profiles due to the strain tunability of electron−phonon interactions in BP thin films. For a fixed crystallographic orientation, Raman intensity of BP is sensitive to laser wavelength, substrate insulator stack, and sample thickness.[23] Interference effects due to the reflection and transmission of Raman scattered light at interfaces between the sample, substrate, and capping layers were calculated via a procedure similar to that outlined in reports by Yoon et al. and Kim et al.[30,43] These effects can alter the anisotropic Raman response of birefringent materials, resulting in a polarization dependence of Raman spectra that is not strictly due to intrinsic material

DOI: 10.1021/acsnano.8b06940
ACS Nano 2018, 12, 12512−12522

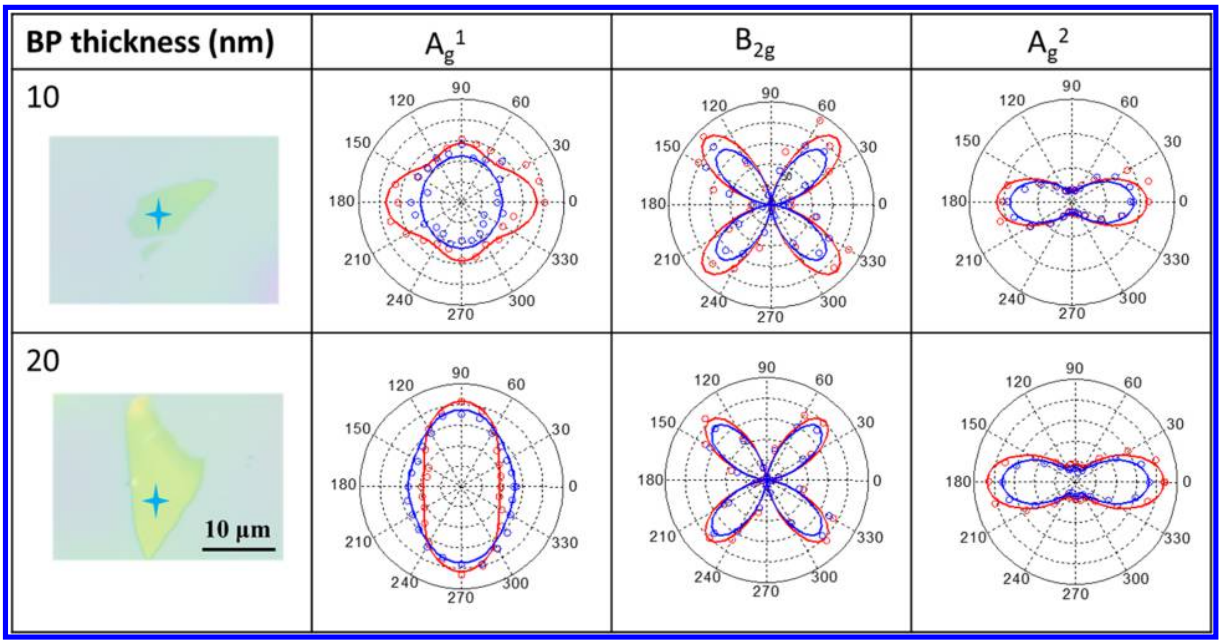

Figure 5. Under tensile strain along the AC direction, distinct angle-resolved Raman intensity evolution was observed in BP samples with different thicknesses. The red line and dots are the data collected for a relaxed sample under no stain. The blue line and dots are the date collected for the sample under 1% strains. The dots are experimental data, and the lines are model fitting results. 0° is defined along the AC direction in the polar plot.

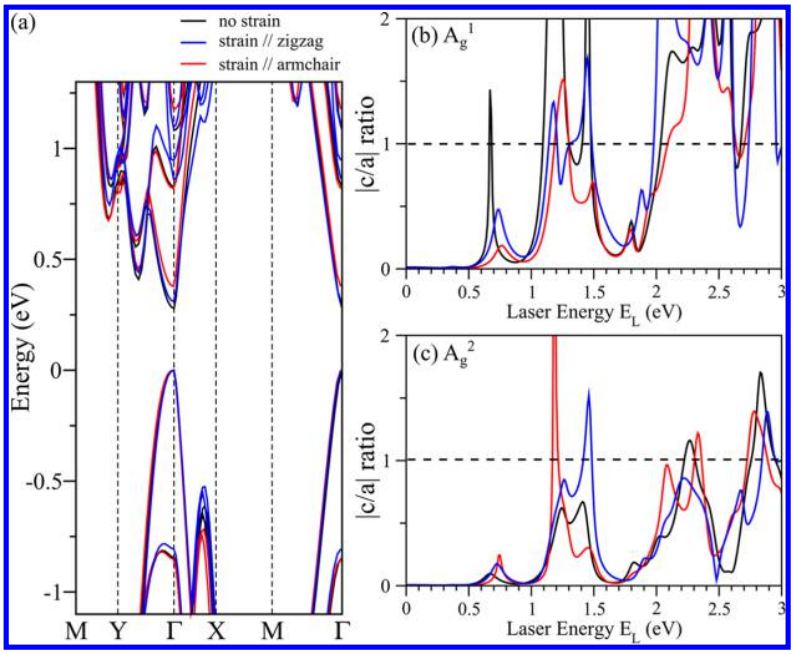

Figure 6. For bilayer BP under no strain (black lines), 1.7% tensile strain along the zigzag direction (blue lines), and 1.7% tensile strain along the armchair direction (red lines), panel a shows DFT calculated electronic band structures, while panels b and c show calculated Raman tensor element ratios $|c/a|$ as a function of excitation laser energy for A_g^1 and A_g^2 modes, respectively. Note that DFT tends to underestimate electronic band gaps, and thus, the computed laser energy here cannot be directly compared to the experimental value.

properties. In such cases, the interference factors for light polarized along different crystallographic directions of a birefringent material must be calculated and corrected for. Details of this analysis are available in the Supporting Information. For our sample configuration, it was determined that interference effects are negligible due to the relatively small differences between the refractive indices air, poly(methyl methacrylate) (PMMA), nanopolyimide (NPI), Pd, and polyimide (PI) substrates.

Among the three characteristic Raman peaks (A_g^1, A_g^2, and B_{2g} modes), an interesting thickness-dependent intensity profile evolution has been observed for the A_g^1 mode when tensile strain is applied along either AC or ZZ directions. The angle-resolved Raman intensity profiles under tensile strain along ZZ and AC directions for BP samples with different

DOI: 10.1021/acsnano.8b06940
ACS Nano 2018, 12, 12512−12522

thickness were presented in Figures 4 and 5. To better evaluate the Raman intensity profile evolution, extracted $|c/a|$ values for all strained BP samples and for both A_g^1 and A_g^2 modes are included in the Supporting Information Table S1. Shown in Figure 4 are angle-resolved Raman plots for strain along ZZ direction. Here, two samples with distinct thickness were investigated with thicker samples (>20 nm) used as the bulk reference. The two BP thin-film samples were transferred onto the same polymeric NPI substrate and were therefore subject to the same strain loading and interference environment. The Raman intensity profiles of the relaxed (unstrained) samples (*i.e.*, red circles and lines in Figure 4) validated the thickness difference according to the previous analysis. The $|c/a|$ ratio for the thinner and thicker sample was 0.91 and 3.13, respectively. Under 1.7% of tensile strain loading along ZZ direction (blue circles and lines), the dumbbell shape with main axis along ZZ direction reoccurred for the thinner sample, as shown in Figure 4 for the A_g^1 mode ($|c/a|=2.02 > 1$). In contrast, $|c/a|=2.51 > 1$ was extracted for the A_g^1 mode in the thicker sample under ~2% strain, and the dumbbell shape was well-preserved with only intensity reduction.

A similar effect of strain on electron−phonon interactions in thinner BP samples was observed when the uniaxial tensile strain loading was along the AC direction, as shown in Figure 5. For the relaxed thinner sample, A_g^1 mode $|c/a|=0.88 < 1$. At a relatively small tensile strain of ~1%, the axis of highest intensity shifted from the ZZ to the AC ($|c/a|=1.06 > 1$) direction for A_g^1 mode in the thinner sample. A different response in the thicker sample was observed in which the extracted $|c/a|$ ratio is always >1 A_g^1 mode under tensile strain loading up to 2.2%. More experimental results for higher strain loading are shown in the Supporting Information Table S1, where under ~3% of tensile strain, the $|c/a|$ ratio of A_g^1 mode for thinner samples is restored to >1.

To understand the change of electron−phonon interactions in few-layer BP thin films under strain, we first calculated the electronic band structures of unstrained and strained bilayer BP. As shown in Figure 6a, the 1.7% tensile strain loading along both the zigzag and the armchair direction gives rise to subtle changes to the eigenvalues, as well as the electronic band gap. Strain also alters the atomic structure and the wave functions of electronic states. Raman tensor elements correspond to the derivative of the dielectric function elements with respect to the vibrational normal coordinates.[42] Strain acts as perturbation to the eigenvalues and wave functions of electronic states and, subsequently, the dielectric function. Furthermore, it also introduces changes to the phonon vibrations, manifested by the frequency changes of Raman modes discussed above. Therefore, it can change Raman tensor elements and their ratios as well. DFT calculations shown in Figure 6b,c confirm that the ratios $|c/a|$ of A_g^1 and A_g^2 modes indeed vary with strain and, more importantly, the degree of variation is different for the ZZ- and AC-direction strains, highlighting the in-plane anisotropy of electron−phonon interactions in BP. As discussed, the Raman intensity polarization profiles of the A_g modes are primarily determined by the ratio $|c/a|$, in which the Raman tensor element c and a correspond to the ZZ and AC directions, respectively. The value of $|c/a|$ determines whether the maximum intensity direction is along the AC ($|c/a| < 1$) or ZZ ($|c/a| > 1$) directions. When $|c/a|$ approaches 1, a circular profile is present. The changes of $|c/a|$ for A_g^1 and A_g^2 modes under strain in Figure 6 indicate the subsequent changes of Raman intensity polarization profiles that are experimentally observed in Figures 4 and 5.

More specifically, for the A_g^2 mode at most laser energies in Figure 6c, the calculations suggest $|c/a| < 1$ because its atomic displacements are primarily along armchair direction that generally leads to larger Raman tensor element in the AC direction (a) than in the ZZ direction (c).[23] For subtle perturbation by strain, $|c/a|$ of the A_g^2 mode generally remains <1. This explains why in Figures 4 and 5, for both thin and thick samples under no strain and under strain, the $|c/a|$ value of the A_g^2 mode is always <1, and thus, the polarization profiles do not change dramatically. In contrast, for the A_g^1 mode corresponding to out-of-plane atomic vibrations, it does not show notable preference to the in-plane Raman tensor elements a and c, and its ratio of $|c/a|$ is more sensitive to parameter change and external perturbation, *i.e.*, the ratio can be <1 or >1 depending on the sample thickness, laser energy, and strain.[23,42,43] Indeed, as illustrated in Figures 4 and 5 (also Table S1), $|c/a|$ switches from <1 to >1 from the unstrained thin to thick sample. Furthermore, its ratio also fluctuates under and above 1 at different laser energies in Figure 6b (black line). In addition, our calculations in Figure 6b suggest that $|c/a|$ of the A_g^1 mode can be altered from <1 to >1 by strain or vice versa. These results shed light on why, in Figures 4 and 5, $|c/a|$ of the A_g^1 mode and its polarization profiles can exhibit notable changes under strain. In particular, for the unstrained thin sample, $|c/a|$ of the A_g^1 mode is smaller than but close to 1, and hence, strain changes the ratio to >1, resulting in dramatic changes in the polarization profiles.

CONCLUSIONS

In summary, we uncover that the Poisson's ratio is one of the critical parameters affecting frequency changes under strain, which shed light on the pre-existing inconsistency of Raman peak shift under tensile strain in literature. Our work finds that the frequencies of A_g^1, B_{2g}, and A_g^2 modes have the opposite response to the tensile strain along zigzag and armchair directions. Even under the same uniaxial strain, A_g^1 shows the opposite behavior to B_{2g} and A_g^2 modes. This is attributed to the in-plane puckered crystalline structure of BP. Together with angle-resolved Raman spectroscopy, the thickness-sensitive anisotropic electron−phonon interactions in strained few-layer BP thin films are investigated. Our angle-resolved Raman spectroscopy and DFT Raman simulations reveal that the anisotropy of A_g Raman modes depends on the BP sample thickness, excitation laser wavelength, and strain. The $|c/a|$ ratio and polarization profile of the A_g^1 mode are more sensitive to external perturbations and can be utilized to detect/gauge the strain loading. However, the $|c/a|$ ratio of the A_g^2 mode tends to be <1 regardless of the changes in sample thickness and the strain loading. Thus, its polarization profile can be more reliably used to identify the crystallographic orientation. This thickness sensitive electron−phonon interaction with strong in-plain anisotropy under strain makes few-layer black phosphorus promising candidate for electronics and photonics applications.

METHODS

Sample Preparations. BP thin films were mechanically exfoliated using ultratape from the bulk BP single crystal, which was purchased from the vendor HQ Graphene. For unstrained sample experiments, highly P-type doped Si with atomic layer deposited (ALD) Al_2O_3 (25 nm) was employed as the substrate. PMMA A4 was immediately spin-

DOI: 10.1021/acsnano.8b06940
ACS Nano 2018, 12, 12512−12522

coated after mechanical exfoliation as the encapsulation layer for improving ambient stability of BP thin films. BP thin films with thickness ranging from 3 to 20 nm were then located using Olympus microscope.

NPI Substrate Preparation. Commercially available polyimide thin films with initial thickness of 1 mil (~27.5 μm) was requested from Dupont as the stretchable substrate. After the double-sided curing process, in which liquid polyimide was spin-coated and cured in N_2 oven at 300 °C, the PI substrate was smooth with surface roughness of <2 nm. A Pd-to-Cr ratio of 50/3 nm was deposited on top of the PI substrate as the metal stack for enhancing optical contrast. *N*-Methyl-2-pyrrolidone (NMP)-diluted liquid polyimide was then spin-coated at a speed of 6000 rpm to achieve a thin film down to 60 nm after curing process in N_2 oven at 300 °C. Scanning electron microscope (SEM) alignment marks were created to help locate the BP sample.

Tensile Strain Loading. A homemade stretching fixture was used for the tensile strain loading, in which the long stripe-shaped PI substrate was mounted across the two clamps of the stretcher. The initial end to end distance between the two clams was measured with a caliper and then used as the initial length for strain calculations.

Raman Characterization. Raman spectra were measured in a back-scattering configuration using a commercial Renishaw inVia micro-Raman system and a 45 mW (maximum) 473 nm wavelength laser. The incident laser had an established polarization angle with respect to the samples, and only polarizations parallel to the incident beam polarization were collected. To ensure that the incident beam was normal to the plane of BP, polarized Raman plots were calibrated against previous reports in literature, ensuring that the proper projection of the Raman tensor (the projection in the ZZ−AC plane) was being measured. The samples were rotated with respect to the incident polarization via a motorized continuous rotation stage (ThorLabs PRMTZ8) with 5-arcmin resolution and ±0.2° locating precision using a DC servo motor controller (ThorLabs KDC101). All spectra were measured under 50× magnification, resulting in a beam spot ~1 μm in diameter. For Raman measurements, a spectrum resolution of ~1 cm^{-1} was achieved using a 2400 lines/mm grating.

DFT Calculations. Plane-wave density functional theory (DFT) calculations were carried out using the VASP software with projector augmented wave (PAW) pseudopotentials for electron−ion interactions[44] and the Perdew−Burke−Ernzerhof (PBE) functional for exchange-correlation interactions.[45] van der Waals (vdW) interactions were included using the vdW density functional method optB86b-vdW.[46] For bulk BP, both atoms and cell volume were allowed to relax until the residual forces below 0.001 eV/Å, with a cutoff energy set at 500 eV and a 9 × 4 × 12 k-point sampling.[41] Here we defined the *X* axis as the in-plane armchair direction, the *Y* axis as the out-of-plane direction, and the *Z* axis as the in-plane zigzag direction.[23,42] Monolayer and bilayer BP systems were then modeled by a periodic slab geometry, in which a vacuum separation of 22 Å in the out-of-plane direction was used to avoid spurious interactions with periodic images. For the 2D slab calculations, 9 × 1 × 12 k-point samplings were used, and all atoms were relaxed until the residual forces were below 0.001 eV/Å and the in-plane lattice constants were also optimized. For the optimized monolayer, bilayer and bulk BP, uniaxial tensile strains of 1.7% and 3.4% were introduced along the armchair or zigzag direction, and then all atoms were again relaxed. Note that when the strain was applied to one in-plane direction, the lattice constant along the other in-plane direction was also changed and, hence, optimized as well.

Phonon and Raman tensor calculations were performed using the optimized structures. The dynamic matrix was calculated using the finite difference scheme implemented in the Phonopy software.[47] Hellmann−Feynman forces in the 3 × 1 × 3 supercell were computed by VASP for both positive and negative atomic displacements (δ = 0.03 Å) and then used in Phonopy to construct the dynamic matrix, whose diagonalization provides phonon frequencies and phonon eigenvectors (*i.e.*, vibrations). For the *j*th phonon mode, the matrix element of the (3 × 3) Raman tensor $\tilde{R}$ is $\tilde{R}_{\alpha\beta}(j) = \frac{V_0}{4\pi}\sum_{\mu=1}^{N}\sum_{l=1}^{3}\frac{\partial\chi_{\alpha\beta}}{\partial r_l(\mu)}\frac{e_l^j(\mu)}{\sqrt{M_\mu}}$, where $\chi_{\alpha\beta}$ is the complex dielectric tensor depending on the excitation laser energy, $r_l(\mu)$ is the position of the μth atom along the direction l, $\frac{\partial\chi_{\alpha\beta}}{\partial r_l(\mu)}$ is the derivative of the dielectric tensor over the atomic displacement, $\frac{e_l^j(\mu)}{\sqrt{M_\mu}}$ is the eigen displacement of the μth atom along the direction l in the jth phonon mode, $e_l^j(\mu)$ corresponds to the eigenvector of the dynamic matrix, M_μ is the mass of the μth atom, and V_0 is the unit cell volume.[48−50] For both positive and negative atomic displacements (δ = 0.03 Å) in the unit cell, the dielectric tensors $\chi_{\alpha\beta}$ were computed by VASP at the chosen laser energy, and then the derivatives were obtained via the finite difference scheme. Based on the phonon frequencies, phonon eigenvectors, and the derivatives of dielectric tensors, Raman tensor $\tilde{R}$ of any phonon mode at any laser energy can be obtained using our in-house developed Raman modeling package.

ASSOCIATED CONTENT

Supporting Information

The Supporting Information is available free of charge on the ACS Publications website at DOI: 10.1021/acsnano.8b06940.

Figures showing the mechanical robustness of polymeric dielectric-based PI substrate, Raman spectra under tensile strain loading along the armchair and zigzag directions, AFM results, DFT calculations, BP flake analysis, and interference ratios; a table showing thin-film ratios; analysis of interference effect in BP Raman characterization as well as DFT calculations (PDF)

AUTHOR INFORMATION

Corresponding Author

*E-mail: deji@ece.utexas.edu.

ORCID

Weinan Zhu: 0000-0002-0256-3750

Liangbo Liang: 0000-0003-1199-0049

Author Contributions

⊥W.Z. and L.L. contributed equally.

Notes

The authors declare no competing financial interest.

ACKNOWLEDGMENTS

This work is supported in part by National Science Foundation (NSF) award no. 1641073, the NSF National Nanotechnology Coordinated Infrastructure (NNCI), and the NSF-NASCENT Engineering Research Center under Cooperative Agreement no. EEC-1160494. D.A. acknowledges the David and Doris Lybarger Endowed Faculty Fellowship. A portion of this research (theoretical calculations) used resources at the Center for Nanophase Materials Sciences, which is a DOE Office of Science User Facility operated by the Oak Ridge National Laboratory. L.L. was supported by Eugene P. Wigner Fellowship at the Oak Ridge National Laboratory and by the Center for Nanophase Materials Sciences. J.F.L. acknowledges equipment funds from Deep Carbon Observatory and Department of Geological Sciences, Jackson School of Geosciences at University of Texas at Austin for the purchase and operation of the Renishaw Raman system in his Mineral Physics laboratory.

DOI: 10.1021/acsnano.8b06940
ACS Nano 2018, 12, 12512−12522

REFERENCES

(1) Liu, H.; Neal, A. T.; Zhu, Z.; Luo, Z.; Xu, X.; Tomanek, D.; Ye, P. D. Phosphorene: An Unexplored 2D Semiconductor With A High Hole Mobility. *ACS Nano* **2014**, *8*, 4033−4041.

(2) Li, L.; Yu, Y.; Ye, G. J.; Ge, Q.; Ou, X.; Wu, H.; Feng, D.; Chen, X. H.; Zhang, Y. Black Phosphorus Field-Effect Transistors. *Nat. Nanotechnol.* **2014**, *9*, 372−377.

(3) Xia, F.; Wang, H.; Jia, Y. Rediscovering Black Phosphorus as An Anisotropic Layered Material for Optoelectronics and Electronics. *Nat. Commun.* **2014**, *5*, 4458−4463.

(4) Castellanos-Gomez, A.; Vicarelli, L.; Prada, E.; Island, J. O.; Narasimha-Acharya, K. L.; Blanter, S. I.; Groenendijk, D. J.; Buscema, M.; Steele, G. A.; Alvarez, J. V.; Zandbergen, H. W.; Palacios, J. J.; van der Zant, H. S. J. Isolation and Characterization of Few-Layer Black Phosphorus. *2D Mater.* **2014**, *1*, 025001−025019.

(5) Qiao, J.; Kong, X.; Hu, Z. X.; Yang, F.; Ji, W. High-Mobility Transport Anisotropy and Linear Dichroism in Few-Layer Black Phosphorus. *Nat. Commun.* **2014**, *5*, 4475−4481.

(6) Wang, X.; Jones, A. M.; Seyler, K. L.; Tran, V.; Jia, Y.; Zhao, H.; Wang, H.; Yang, L.; Xu, X.; Xia, F. Highly Anisotropic and Robust Excitons in Monolayer Black Phosphorus. *Nat. Nanotechnol.* **2015**, *10*, 517−521.

(7) Kim, J. S.; Liu, Y.; Zhu, W.; Kim, S.; Wu, D.; Tao, L.; Dodabalapur, A.; Lai, K.; Akinwande, D. Toward Air-Stable Multilayer Phosphorene Thin-Films and Transistors. *Sci. Rep.* **2015**, *5*, 8989−8995.

(8) Wood, J. D.; Wells, S. A.; Jariwala, D.; Chen, K. S.; Cho, E.; Sangwan, V. K.; Liu, X.; Lauhon, L. J.; Marks, T. J.; Hersam, M. C. Effective Passivation of Exfoliated Black Phosphorus Transistors Against Ambient Degradation. *Nano Lett.* **2014**, *14*, 6964−6970.

(9) Chen, X.; Wu, Y.; Wu, Z.; Han, Y.; Xu, S.; Wang, L.; Ye, W.; Han, T.; He, Y.; Cai, Y.; Wang, N. High-Quality Sandwiched Black Phosphorus Heterostructure and Its Quantum Oscillations. *Nat. Commun.* **2015**, *6*, 7315−7320.

(10) Zhu, W.; Yogeesh, M. N.; Yang, S.; Aldave, S. H.; Kim, J. S.; Sonde, S.; Tao, L.; Lu, N.; Akinwande, D. Flexible Black Phosphorus Ambipolar Transistors, Circuits and AM Demodulator. *Nano Lett.* **2015**, *15*, 1883−1890.

(11) Zhu, W.; Park, S.; Yogeesh, M. N.; McNicholas, K. M.; Bank, S. R.; Akinwande, D. Black Phosphorus Flexible Thin Film Transistors at Gighertz Frequencies. *Nano Lett.* **2016**, *16*, 2301−2306.

(12) Park, S.; Zhu, W.; Chang, H.-Y.; Yogeesh, M. N.; Ghosh, R.; Banerjee, S. K.; Akinwande, D. In *High-Frequency Prospects of 2D Nanomaterials for Flexible Nanoelectronics From Baseband to Sub-THZ Devices*; IEEE: Piscataway, New Jersey, 2015; pp 32.1.1−32.1.4.

(13) Zhang, X.; Xie, H.; Liu, Z.; Tan, C.; Luo, Z.; Li, H.; Lin, J.; Sun, L.; Chen, W.; Xu, Z.; Xie, L.; Huang, W.; Zhang, H. Black Phosphorus Quantum Dots. *Angew. Chem., Int. Ed.* **2015**, *54*, 3653−3657.

(14) Feng, Q.; Yan, F.; Luo, W.; Wang, K. Charge Trap Memory Based on Few-Layer Black Phosphorus. *Nanoscale* **2016**, *8*, 2686−2692.

(15) Buscema, M.; Groenendijk, D. J.; Blanter, S. I.; Steele, G. A.; van der Zant, H. S.; Castellanos-Gomez, A. Fast and Broadband Photoresponse of Few-Layer Black Phosphorus Field-Effect Transistors. *Nano Lett.* **2014**, *14*, 3347−3352.

(16) Youngblood, N.; Chen, C.; Koester, S. J.; Li, M. Waveguide-Integrated Black Phosphorus Photodetector With High Responsivity and Low Dark Current. *Nat. Photonics* **2015**, *9*, 247−252.

(17) Hook, T. B.; Ma, T. Hot-Electron Induced Interface Traps in Metal/Sio_2/Si Capacitors: The Effect of Gate-Induced Strain. *Appl. Phys. Lett.* **1986**, *48*, 1208−1210.

(18) Verheyen, P.; Collaert, N.; Rooyackers, R.; Loo, R.; Shamiryan, D.; De Keersgieter, A.; Eneman, G.; Leys, F.; Dixit, A.; Goodwin, M.; Yim, Y. S.; Caymax, M.; De Meyer, K.; Absil, P.; Jurczak, M.; Biesemans, S. In *25% Drive Current Improvement for P-Type Multiple Gate FET(MugFET) Devices by The Introduction of Recessed Si0.8Ge0.2 in The Source and Drain Regions*; VLSI Technology: San Jose, CA, 2005; pp 194−195.

(19) Liow, T.-Y.; Tan, K.-M.; Lee, R. T.; Du, A.; Tung, C.-H.; Samudra, G. S.; Yoo, W.-J.; Balasubramanian, N.; Yeo, Y.-C. In *Strained n-Channel Finfets With 25 Nm Gate Length and Silicon-Carbon Source/Drain Regions Ffor Performance Enhancement*; VLSI Technology: San Jose, CA, 2006; pp 56−57.

(20) Gui, G.; Li, J.; Zhong, J. Band Structure Engineering of Graphene by Strain: First-Principles Calculations. *Phys. Rev. B: Condens. Matter Mater. Phys.* **2008**, *78*, 075435−6.

(21) Lu, Y.; Guo, J. Band Gap of Strained Graphene Nanoribbons. *Nano Res.* **2010**, *3*, 189−199.

(22) Yeh, W. K.; Wang, C. C.; Hsu, C. W.; Fang, Y. K.; Wu, S. M.; Ou, C. C.; Lin, C. L.; Gan, K. J.; Weng, C. J.; Chen, P. Y.; Jiann-Shiun, Y.; Liou, J. J. In *Impact of Oxide Trap Charge on Performance of Strained Fully Depleted SOI Metal-Gate MOSFET*; IEEE: Piscataway, NJ, 2009; pp 197−200.

(23) Ling, X.; Huang, S.; Hasdeo, E. H.; Liang, L.; Parkin, W. M.; Tatsumi, Y.; Nugraha, A. R.; Puretzky, A. A.; Das, P. M.; Sumpter, B. G.; Geohegan, D. B.; Kong, J.; Saito, R.; Drndic, M.; Meunier, V.; Dresselhaus, M. S. Anisotropic Electron-Photon and Electron-Phonon Interactions in Black Phosphorus. *Nano Lett.* **2016**, *16*, 2260−2267.

(24) Wei, Q.; Peng, X. H. Superior Mechanical Flexibility of Phosphorene and Few-Layer Black Phosphorus. *Appl. Phys. Lett.* **2014**, *104*, 251915−5.

(25) Fei, R.; Yang, L. Strain-Engineering the Anisotropic Electrical Conductance of Few-Layer Black Phosphorus. *Nano Lett.* **2014**, *14*, 2884−2889.

(26) Peng, X. H.; Wei, Q.; Copple, A. Strain-Engineered Direct-Indirect Band Gap Transition and Its Mechanism in Two-Dimensional Phosphorene. *Phys. Rev. B: Condens. Matter Mater. Phys.* **2014**, *90*, 085402−10.

(27) Fei, R.; Yang, L. Lattice Vibrational Modes and Raman Scattering Spectra of Strained Phosphorene. *Appl. Phys. Lett.* **2014**, *105*, 083120−4.

(28) Liu, Z.; Amani, M.; Najmaei, S.; Xu, Q.; Zou, X.; Zhou, W.; Yu, T.; Qiu, C.; Birdwell, A. G.; Crowne, F. J.; Vajtai, R.; Yakobson, B. I.; Xia, Z.; Dubey, M.; Ajayan, P. M.; Lou, J. Strain and Structure Heterogeneity in MoS_2 Atomic Layers Grown by Chemical Vapour Deposition. *Nat. Commun.* **2014**, *5*, 5246−9.

(29) Chang, H. Y.; Yang, S.; Lee, J.; Tao, L.; Hwang, W. S.; Jena, D.; Lu, N.; Akinwande, D. High-Performance, Highly Bendable MoS_2 Transistors With High-K Dielectrics for Flexible Low-Power Systems. *ACS Nano* **2013**, *7*, 5446−5452.

(30) Yoon, D.; Moon, H.; Son, Y.; Choi, J.; Park, B.; Cha, Y. H.; Kim, Y. D.; Cheong, H. Interference Effect on Raman Spectrum of Graphene on SiO_2/Si. *Phys. Rev. B: Condens. Matter Mater. Phys.* **2009**, *80*, 125422−6.

(31) Park, S.; Chang, C. Y.; Rahimi, S.; Lee, A.; Akinwande, D. In *Flexible 2D Electronics Using Nanoscale Transparent Polyimide Gate Dielectric*; Device Research Conference (DRC), IEEE, 2015 73rd Annual, 21−24 June 2015; 2015; pp 193−194. DOI: 10.1109/DRC.2015.7175628, https://ieeexplore.ieee.org/abstract/document/7175628.

(32) Tao, J.; Shen, W.; Wu, S.; Liu, L.; Feng, Z.; Wang, C.; Hu, C.; Yao, P.; Zhang, H.; Pang, W.; Duan, X.; Liu, J.; Zhou, C.; Zhang, D. Mechanical and Electrical Anisotropy of Few-Layer Black Phosphorus. *ACS Nano* **2015**, *9*, 11362−113670.

(33) Wang, Y.; Cong, C.; Fei, R.; Yang, W.; Chen, Y.; Cao, B.; Yang, L.; Yu, T. Remarkable Anisotropic Phonon Response in Uniaxially Strained Few-Layer Black Phosphorus. *Nano Res.* **2015**, *8*, 3944−3953.

(34) Zhang, S.; Mao, N.; Wu, J.; Tong, L.; Zhang, J.; Liu, Z. In-Plane Uniaxial Strain in Black Phosphorus Enables the Identification of Crystalline Orientation. *Small* **2017**, *13*, 1700466.

(35) Li, Y.; Hu, Z.; Lin, S.; Lai, S.; Ji, W.; Lau, S. P. Giant Anisotropic Raman Response of Encapsulated Ultrathin Black Phosphorus by Uniaxial Strain. *Adv. Funct. Mater.* **2017**, *27*, 1600986−9.

DOI: 10.1021/acsnano.8b06940
ACS Nano 2018, 12, 12512−12522

(36) Du, Y.; Maassen, J.; Wu, W.; Luo, Z.; Xu, X.; Ye, P. D. Auxetic Black Phosphorus: A 2D Material with Negative Poisson's Ratio. *Nano Lett.* **2016**, *16*, 6701−6708.
(37) Rice, C.; Young, R. J.; Zan, R.; Bangert, U.; Wolverson, D.; Georgiou, T.; Jalil, R.; Novoselov, K. S. Raman-Scattering Measurements and First-Principles Calculations of Strain-Induced Phonon Shifts in Monolayer MoS_2. *Phys. Rev. B: Condens. Matter Mater. Phys.* **2013**, *87*, 081307−5.
(38) Wu, J.; Mao, N.; Xie, L.; Xu, H.; Zhang, J. Identifying The Crystalline Orientation of Black Phosphorus Using Angle-Resolved Polarized Raman Spectroscopy. *Angew. Chem., Int. Ed.* **2015**, *54*, 2366−2369.
(39) Mao, N.; Zhang, S.; Wu, J.; Zhang, J.; Tong, L. Lattice Vibration and Raman Scattering in Anisotropic Black Phosphorus Crystals. *Small Methods* **2018**, *2*, 1700409.
(40) Ribeiro, H. B.; Pimenta, M. A.; de Matos, C. J. S. Raman Spectroscopy in Black Phosphorus. *J. Raman Spectrosc.* **2018**, *49*, 76−90.
(41) Ling, X.; Liang, L.; Huang, S.; Puretzky, A. A.; Geohegan, D. B.; Sumpter, B. G.; Kong, J.; Meunier, V.; Dresselhaus, M. S. Low-Frequency Interlayer Breathing Modes in Few-Layer Black Phosphorus. *Nano Lett.* **2015**, *15*, 4080−4088.
(42) Ribeiro, H. B.; Pimenta, M. A.; de Matos, C. J.; Moreira, R. L.; Rodin, A. S.; Zapata, J. D.; de Souza, E. A.; Castro Neto, A. H. Unusual Angular Dependence of The Raman Response in Black Phosphorus. *ACS Nano* **2015**, *9*, 4270−4276.
(43) Kim, J.; Lee, J. U.; Lee, J.; Park, H. J.; Lee, Z.; Lee, C.; Cheong, H. Anomalous Polarization Dependence of Raman Scattering and Crystallographic Orientation of Black Phosphorus. *Nanoscale* **2015**, *7*, 18708−15.
(44) Kresse, G.; Furthmüller, J. Efficiency of Ab-Initio Total Energy Calculations for Metals and Semiconductors Using a Plane-Wave Basis Set. *Comput. Mater. Sci.* **1996**, *6*, 15−50.
(45) Perdew, J. P.; Burke, K.; Ernzerhof, M. Generalized Gradient Approximation Made Simple. *Phys. Rev. Lett.* **1996**, *77*, 3865−3868.
(46) Dion, M.; Rydberg, H.; Schroder, E.; Langreth, D. C.; Lundqvist, B. I. Van Der Waals Density Functional For General Geometries. *Phys. Rev. Lett.* **2004**, *92*, 246401−4.
(47) Togo, A.; Oba, F.; Tanaka, I. First-Principles Calculations of The Ferroelastic Transition Between Rutile-Type and $CaCl_2$-Type SiO_2 at High Pressures. *Phys. Rev. B: Condens. Matter Mater. Phys.* **2008**, *78*, 134106−9.
(48) Umari, P.; Pasquarello, A.; Dal Corso, A. Raman Scattering Intensities in A-Quartz: a First-Principles Investigation. *Phys. Rev. B: Condens. Matter Mater. Phys.* **2001**, *63*, 094305−9.
(49) Liang, L.; Meunier, V. First-Principles Raman Spectra Of MoS_2, WS_2 and Their Heterostructures. *Nanoscale* **2014**, *6*, 5394−5401.
(50) Talirz, L.; Sode, H.; Dumslaff, T.; Wang, S.; Sanchez-Valencia, J. R.; Liu, J.; Shinde, P.; Pignedoli, C. A.; Liang, L.; Meunier, V.; Plumb, N. C.; Shi, M.; Feng, X.; Narita, A.; Mullen, K.; Fasel, R.; Ruffieux, P. On-Surface Synthesis and Characterization of 9-Atom Wide Armchair Graphene Nanoribbons. *ACS Nano* **2017**, *11*, 1380−1388.

DOI: 10.1021/acsnano.8b06940
ACS Nano 2018, 12, 12512−12522